RSC Advances

PAPER

View Article Online
View Journal | View Issue

Check for updates

Cite this: *RSC Adv.*, 2025, **15**, 50076

Efficient dye removal using well-crystallized layered double hydroxides and their oxides: insights into kinetics, thermodynamics, isotherm and the memory effect

Saleem Reihana Parveen [ab] and Viruthachalam Thiagarajan [*ab]

Dyes are toxic organic compounds that can adversely affect living organisms, and their removal from wastewater is a critical environmental concern. This study primarily focuses on the synthesis and adsorption behavior towards both cationic and anionic dyes of well-crystallized Mg–Al layered double hydroxides (MAH), made using highly concentrated metal salts, and their thermally treated derivatives, Mg–Al layered double oxides (MAO). Whilst both MAH and MAO exhibit high adsorption capacities for the methyl orange (MO) and acid blue 113 (AB) dyes, MAO, however, demonstrates slightly greater adsorption efficiency due to its increased surface area resulting from calcination. The adsorption behavior of these nanocomposites was studied by varying parameters such as contact time, temperature, pH, ionic strength, initial dye concentration and adsorbent dosage. The adsorption kinetics were best described by a pseudo second order model. Thermodynamic parameters such as the enthalpy, entropy and Gibb's free energy were calculated and the negative value for the free energy confirms the spontaneity and feasibility of the process, while the negative value of ΔH indicates that the adsorption process is physisorption and exothermic in nature. Two of the most widely used adsorption isotherms, the Freundlich and Langmuir models, were applied to fit the data. Both materials exhibited a good fit with the Langmuir model. The memory effect of MAO was studied by allowing the material to rehydrate to its LDH structure by moisture absorption from the environment over different durations (in days) followed by examining its adsorption behavior towards the MO dye. The reusability of the MAO material for MO dye adsorption was tested over multiple cycles, with washing between each cycle using solvents, acids, and bases. Additionally, the MO dye desorbed from the MAO material remained chemically intact and was recovered after washing the adsorbent with ethanol. This study demonstrates that both the adsorbent and the adsorbate materials are reusable.

Received 4th September 2025
Accepted 30th November 2025

DOI: 10.1039/d5ra06650f

rsc.li/rsc-advances

Open Access Article. Published on 15 December 2025. Downloaded on 4/9/2026 11:37:07 PM.
This article is licensed under a Creative Commons Attribution-NonCommercial 3.0 Unported Licence.

1. Introduction

Water, the most abundant and fundamental resource on Earth, is a basic component of life and ecosystems and plays a major role in supporting diverse habitats and maintaining the planet's climate. Regardless of its abundance on Earth, the availability and quality of the water is under threat due to anthropogenic activities.[1] These anthropogenic activities include textile manufacturing, paper production, printing, food coloring, cosmetics production, the leather tanning industry, *etc.*, and lead to the discharge of synthetic dyes that contaminate water. These synthetic dyes are harmful to human health causing cancer risk, respiratory and neurological damage and also, they affect aquatic species by disrupting their food chain. Among the various synthetic dyes used, the anionic dyes methyl orange and acid blue 113 are the most vivid in color and are widely found in industrial effluents, which cause severe environmental damage. To remove these dyes from wastewater, several physical and chemical methods like adsorption, membrane filtration, coagulation, flocculation, advanced oxidation, chemical reduction, electrochemical treatments, biodegradation and enzymatic treatments are available.[2–4] Among these available techniques, adsorption is the most simple, cost-effective and widely used method for the removal of organic dyes from wastewater.[5,6] To carry out this adsorption process successful, the selection of a suitable adsorbent plays a crucial role. The adsorbent should possess a high surface area, high chemical stability and a strong affinity for the pollutant. In recent times, layered double hydroxides (LDHs) have been shown to act as classic nano-adsorbent materials for removing toxic pollutants from water.[7–10] These materials have gathered wide interest due to their unique crystallinity and biocompatibility for various

[a]*Photonics and Biophotonics Lab, School of Chemistry, Bharathidasan University, Trichy 620024, Tamil Nadu, India. E-mail: v.thiagarajan@bdu.ac.in*
[b]*Faculty Recharge Programme, University Grants Commission, New Delhi, India*

© 2025 The Author(s). Published by the Royal Society of Chemistry

Open Access Article. Published on 15 December 2025. Downloaded on 4/9/2026 11:37:07 PM.
This article is licensed under a Creative Commons Attribution-NonCommercial 3.0 Unported Licence.

applications in the field of water remediation. LDHs act as inorganic materials and have excellent morphological and physiochemical properties. LDHs are anionic clay materials made of a two-dimensional plate/sheet-like positively charged structure with a large surface area, and anion exchangeability that acts as a cheap application material in various fields.[11–14] The two-dimensional arrangement of these structures contains positively charged layers (divalent and trivalent cations) with hydroxyl groups present on the surface of the layers where water molecules and the anions are intercalated in the interlayer gallery through electrostatic interactions (Scheme S1). The general molecular formula of LDHs can be represented as,

$$\left[M_{1-X}{}^{2+}M_X{}^{3+}(OH_2)\right]\ [A^{n-}]_{\frac{X}{n}}\cdot ZH_2O$$

in which, M^{2+} represents a bivalent cation (Mg^{2+}, Zn^{2+}, Cu^{2+}, Ni^{2+}, *etc.*), M^{3+} represents a trivalent cation (Al^{3+}, Mn^{3+}, Fe^{3+}, *etc.*) and A^{n-} represents the anions present in the interlayer gallery ($NO_3{}^{2-}$, Cl^-, $SO_4{}^{2-}$, $CO_3{}^{2-}$, *etc.*), where X varies from 0.2–0.4 and Z varies from 0.5–1.[15]

Upon thermal treatment *via* a calcination process, the layered double hydroxides are transformed into layered double oxides (LDO). The process involves four different consecutive steps dehydration, dehydroxylation, decomposition of the anions followed by oxide reformation. Initially, the LDHs are calcined at higher temperatures in which the layered structure is destroyed and the water molecules in the interlamellar region are dehydrated followed by dehydroxylation where the hydroxides are converted to oxides and finally end up with the loss of anions in the layer. The layered structure of LDH can be regenerated from LDO by a rehydration process.[16,17] This structural transformation of an LDO into an LDH is called the memory effect.[18–20]

This study reports the synthesis of single-phase, well-crystallized Mg–Al layered double hydroxide (MAH) and its corresponding layered double oxide (MAO) *via* a hydrothermal route that uses highly concentrated metal salt solutions and urea as a precipitating agent. The use of the highest metal ion precursor concentrations in this method promotes homogeneous precipitation and enhanced crystallinity, leading to structurally uniform MAH/MAO materials. MAO demonstrates efficient and pH-independent adsorption of anionic dyes, surpassing previously reported LDH/LDO-based adsorbents across all pH conditions (acidic, neutral, and basic). Furthermore, the "memory effect," *i.e.*, the reconstruction of the LDH structure from the calcined LDO in aqueous media, was confirmed. MAO shows high adsorption capacities toward methyl orange (MO) and acid blue (AB) dyes, demonstrating their effectiveness and environmental relevance for dye-contaminated wastewater treatment.

2. Materials and methods

2.1 Materials

Magnesium chloride and aluminum chloride were purchased from Sisco Research Laboratories Pvt. Ltd (SRL), India. Emparta-grade urea, sodium hydroxide, sodium nitrate and Emsure-grade hydrochloric acid were obtained from Merck, and methyl orange dye was purchased from Alfa Aesar. Acid blue 113, rhodamine B, and rhodamine 6G were procured from Sigma-Aldrich. Adjustments to the pH were made using concentrated hydrochloric acid and sodium hydroxide solutions. Ionic strength variations were studied using different concentrations of sodium nitrate solutions. Double-distilled water was used as the solvent throughout the adsorption studies. The synthesized materials were characterized using several instruments, and the details are provided in the SI.

2.2 Synthesis of MAH and MAO adsorbents

Well-crystallized Mg–Al layered double hydroxides were synthesized using a highly concentrated metal salt solution using urea as a precipitating agent. Initially, $AlCl_3\cdot 6H_2O$ (0.25 M) and $MgCl_2\cdot 6H_2O$ (0.75 M) were dissolved in 35 mL of double-distilled water at a 1 : 3 molar ratio, while urea (2.5 M) was dissolved separately in 25 mL of double-distilled water. Both the aqueous solutions were mixed and stirred using a magnetic stirrer under ambient temperature to get a clear solution. Then, the clear solution was transferred into a 100-mL Teflon-lined autoclave and heated at 8 °C per minute to reach a temperature of 100 °C and was maintained at this temperature for 24 hours.[21] The white solid product synthesized was aged for 4 hours, centrifuged to remove the supernatant solution, washed with double distilled water and dried at 60 °C to obtain the Mg–Al layered double hydroxide (MAH). The synthesized MAH was calcined by increasing the temperature at the rate of 1 °C min^{-1} and maintained at 500 °C for 4 hours. The resultant calcined product formed was a Mg–Al layered double oxide (MAO). A schematic representation of this synthesis is represented in Scheme 1. Compared to conventional LDH synthesis routes that typically employ lower precursor concentrations and higher temperature conditions, this method promotes homogeneous nucleation and growth resulting in well-crystallized and uniform LDH nanocomposites with enhanced adsorption capacities for the anionic dyes.

2.3 Batch adsorption experiments

The bulk dye solutions were prepared using double-distilled water. All batch adsorption experiments were conducted by mixing 25 mL of the desired dye concentration of the solution with 30 mg of the adsorbent, followed by equilibrium shaking at 1200 rpm for one hour. At predetermined time intervals, aliquots of the solution were taken, centrifuged, and the concentration of the remaining dye was determined by measuring the absorbance at the dye's maximum absorption wavelength using a UV-vis spectrophotometer. The representative absorption spectra for the MO dye before and after dye adsorption at different time intervals using MAH and MAO are presented in Fig. S1. The efficiency of the adsorbent was calculated using the formula presented in the SI.

3. Results and discussion

The synthesis of MAH was carried out *via* a hydrothermal process using highly concentrated solutions of magnesium chloride (0.75

Open Access Article. Published on 15 December 2025. Downloaded on 4/9/2026 11:37:07 PM.
This article is licensed under a Creative Commons Attribution-NonCommercial 3.0 Unported Licence.

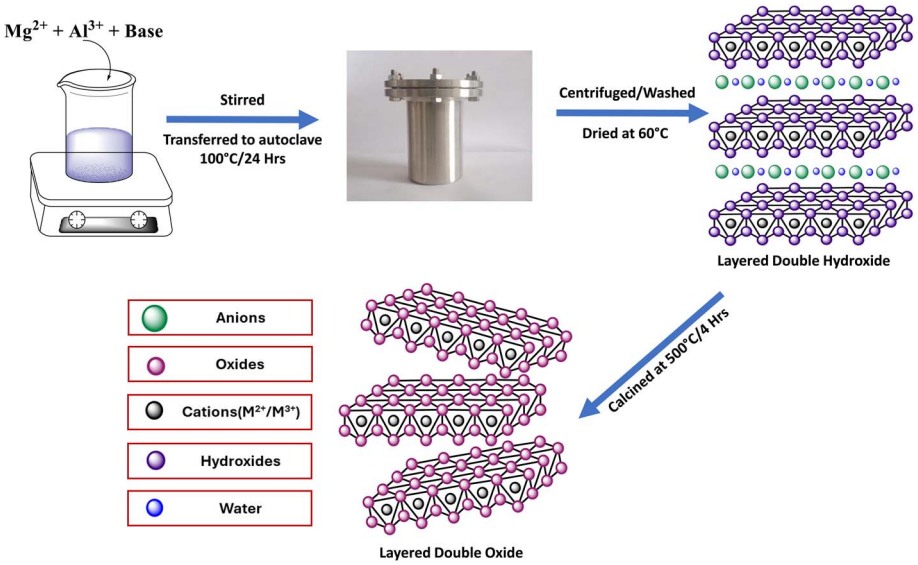

Scheme 1 Syntheses of MAH and MAO.

M) and aluminum chloride (0.25 M) to achieve homogeneous precipitation at a controlled heating rate of 8 °C min^{-1} to reach 100 °C which was maintained for 24 hours. This method yielded well-crystallized single-phase MAH without any by-products such as hydromagnesite or dawsonite.[21] Finally, MAH was calcined at 500 °C to obtain its respective oxide (MAO), as described in the experimental section. The resulting nanocomposites were characterized using powder XRD, FT-IR, SEM, XPS, thermal analysis and surface analysis. The instrumentation used and their details are provided in the SI.

3.1 Characterization of the nanocomposites

To study the crystal structure of MAH and MAO, powder XRD patterns were recorded and are shown in Fig. 1a. MAH shows a pristine hydrotalcite structure with high crystallinity with sharp diffraction peaks at 2θ 11.87°, 23.74°, 35,17°, 39.78°, 47.34°, 61.12° and 62.45° which correspond to the (003), (006), (012), (015), (018), (110) and (113) planes, respectively.[22] Fig. 1a indicates the interlamellar spacing between the layers of MAH.[23] The average crystallite size of MAH was in the range of ~15 nm and the *d*-spacing of the material was calculated using the Scherrer equation represented in Table S1 in the SI. After calcination at 500 °C the crystal structure was destroyed and the layered structure of LDH disappeared completely. The diffraction peak of MAO was observed at $2\theta = 43°$ and 63° showing the formation of the MgO phase.[24] No Al peaks were observed in the pattern as the Al phase may enter the MgO phase.

The FT-IR spectra of MAH and MAO are shown in Fig. 1b. The broad absorption band of LDH at 3406 cm^{-1} corresponds to the stretching frequency of the hydroxyl groups which is attributed to the formation of the hydroxyl groups in the interlamellar region, whereas disappearance of this peak for MAO confirms the loss of the hydroxyl groups after calcination. The intense peak at 1358 cm^{-1} corresponds to the asymmetric

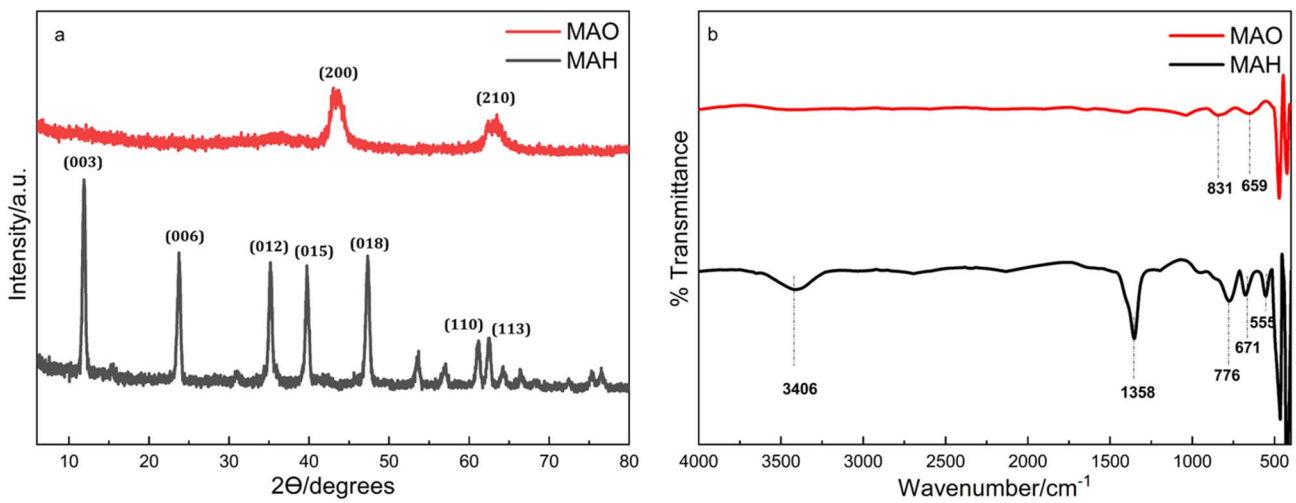

Fig. 1 (a) XRD patterns of MAH and MAO. (b) FT-IR spectra of MAH and MAO.

© 2025 The Author(s). Published by the Royal Society of Chemistry

Open Access Article. Published on 15 December 2025. Downloaded on 4/9/2026 11:37:07 PM.
This article is licensed under a Creative Commons Attribution-NonCommercial 3.0 Unported Licence.

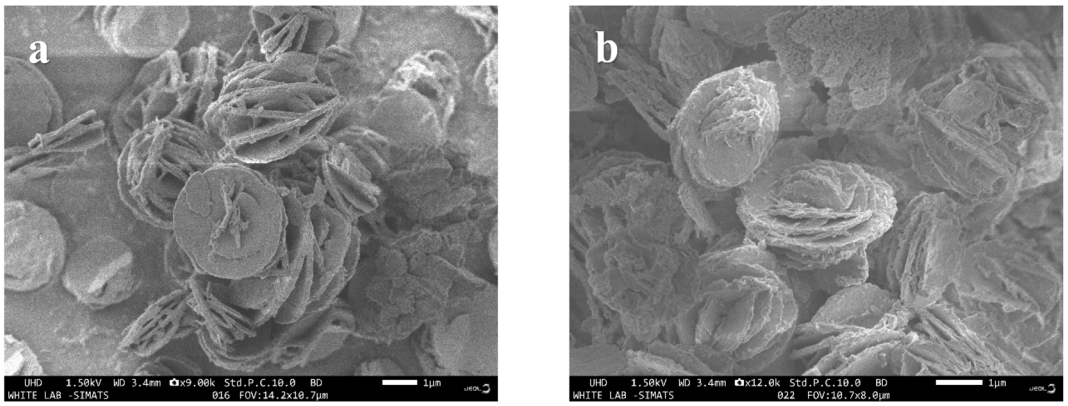

Fig. 2 SEM images of (a) MAH and (b) MAO.

stretching of the carbonate anions. This band disappears after calcination at 500 °C, which indicates the loss of interlayer carbonates between the interlayer region of the MAH material. The bands at 831, 776, 671, 659, and 555 cm^{-1} correspond to the M–O, M–O–M, and M–OH bonds (M = Mg and Al) present on the surface of the LDH and these bands become less intense in the LDO after calcination.[25]

SEM images of MAH and MAO show a flower-like structure with a smooth surface area with an average particle size of 2.4–4.0 μm, as shown in Fig. 2a and b. Even after calcination, the morphology of MAO remains the same as that of MAH, indicating that the calcination did not disturb the morphology of the material. It can be observed that the regular crystal structure has been transformed into amorphous crystals after calcination with an increase in roughness and disorder.[26]

The survey scan of MAH and MAO are shown in Fig. 3 and the elemental composition of the materials can be determined from the XPS data. The peaks for Mg, Al, O and C confirm the presence of these elements in MAH. The deconvolution of the peaks obtained in the spectra helps understand the bonding nature of the ions present in the materials, as shown in Fig. S2. The lattice oxygen 1s spectrum can be deconvoluted into three peaks with maxima at 531, 532, and 533 eV, corresponding to hydroxide ions, carbonate ions, and interlayer water molecules, respectively. The ratio of oxygen present in MAH is higher compared to MAO due to the presence of water molecules in the interlayer. The deconvoluted carbon 1s spectrum is divided into three peaks with maxima of 284, 285 and 289 eV which correspond to the C–C, C–O, and C=O bonds, respectively.[22] In the MAO spectrum, the intensity of the peak at 289 eV is decreased which confirms the decomposition of the interlayer carbonate ions after calcination at 500 °C. The magnesium 1s peak is deconvoluted into 2 peaks at 1304 and 1305 eV which represent $Mg(OH)_3$ and MgO, respectively, and similarly for aluminum 2*p* the deconvoluted peaks at 74 and 75 eV represent the formation of Al $(OH)_3$ and Al_2O_3, respectively.[27]

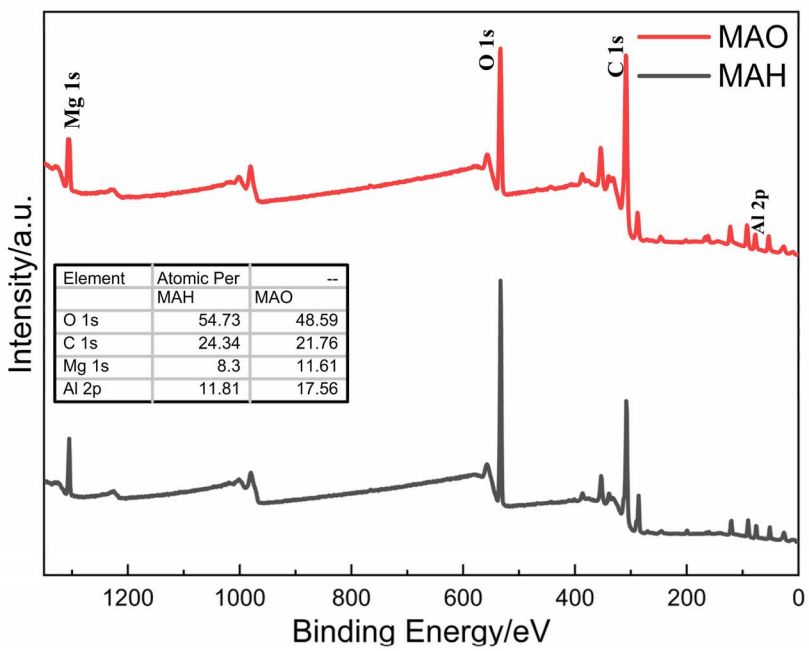

Element	Atomic Per MAH	-- MAO
O 1s	54.73	48.59
C 1s	24.34	21.76
Mg 1s	8.3	11.61
Al 2p	11.81	17.56

Fig. 3 XPS survey scan of MAH and MAO.

Open Access Article. Published on 15 December 2025. Downloaded on 4/9/2026 11:37:07 PM. This article is licensed under a Creative Commons Attribution-NonCommercial 3.0 Unported Licence.

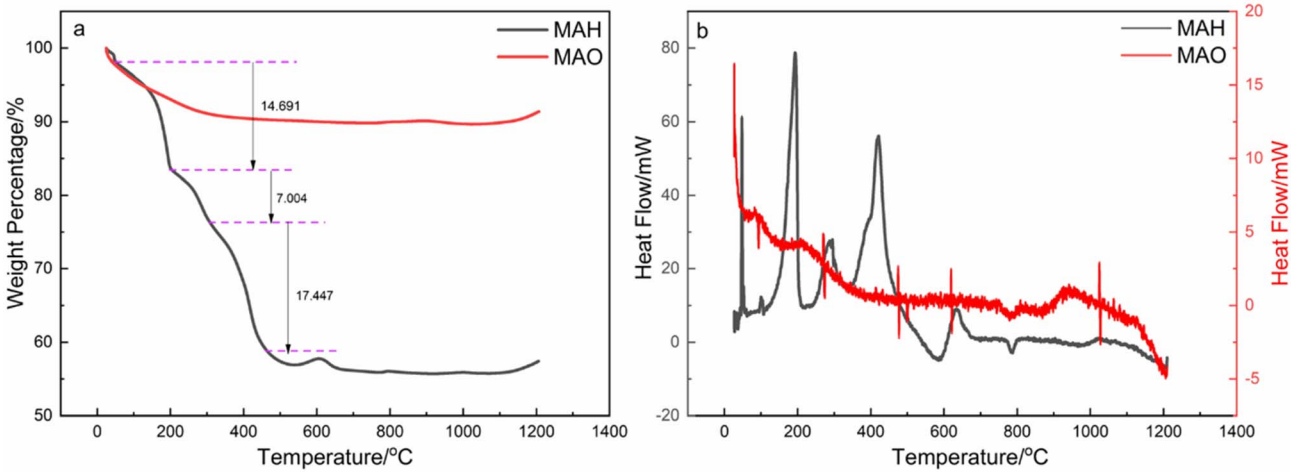

Fig. 4 (a) TGA and (b) DTA curves of MAH and MAO.

The TGA and DTA analysis of MAH and MAO are shown in Fig. 4a and b. Three different mass losses are observed for MAH. The first mass loss of 14.6% occurs between 50–200 °C which is due to the loss of the interlayer water molecules. The second mass loss of 7% around 200–300 °C indicates the occurrence of the dehydroxylation process where the interlayer hydroxyl ions are lost. The third mass loss of 17.4% occurs from 300–480 °C representing the decomposition of the interlayer carbonate anions in which the crystal structure of MAH is destroyed. However, no significant mass loss is observed for MAO, as it has already been calcined at 500 °C and does not undergo decomposition of anions.[22]

The DTA curve of MAH indicates two sharp exothermic decomposition peaks. The first decomposition peak from room temperature to 250 °C indicates the loss of interlayer water molecules whereas the second decomposition peak corresponds to the loss of interlayer anions. For MAO no characteristic peaks were observed since the material is already calcinated at 500 °C.

3.2 Adsorption studies

3.2.1 Adsorption behavior of MAH and MAO towards various dyes. Adsorption studies were performed to evaluate the behavior of MAH and MAO toward anionic and cationic dyes, including methyl orange (MO), acid blue 113 (AB), crystal violet (CV), and rhodamine 6G (R6G). The newly synthesized nanocomposites show higher adsorption for anionic dyes compared to cationic dyes (Fig. S3). MAH showed its highest adsorption percentage for the MO dye whereas MAO showed its highest adsorption percentage for the AB dye, as shown in Fig. 5a and b. Interestingly, MAO shows a higher adsorption percentage for the AB dye at a concentration of 200 mg L^{-1}. Whereas at higher concentrations of adsorbate (500 mg L^{-1}), the adsorption equilibrium of the MO dye on MAO was reached after a shorter contact time than that of the AB dye, as shown in Fig. S4. Thus, the MO dye was selected to study the detailed adsorption kinetics of MAH and MAO under different experimental conditions, such as different initial dye concentrations, contact times, ionic strengths, pHs and adsorbent dosages.

3.2.2 Effect of contact time and initial dye concentration. To study the influence of contact time and initial dye concentration on MO adsorption, different concentrations of MO dye (50, 100, 200, 300 and 500 mg L^{-1}) were chosen to study the adsorption behavior over a time period of up to one hour. On increasing the MO concentration, MAH reaches a maximum percentage of adsorption at 200 mg L^{-1} after which the percentage adsorption decreases when the MO concentration continues to increase, as shown in Fig. S5. At higher MO concentrations (>200 mg L^{-1}), the concentration of MO is higher than the available adsorption sites on MAH which leads to a decrease in the percentage adsorption. In contrast to MAH, the adsorption percentage of MAO shown in Fig. S5 for MO keeps increasing with increases in dye concentrations of up to 500 mg L^{-1}.

The adsorption of MAH increased with contact time, reaching a maximum capacity of 265 mg g^{-1} after 1 hour (Fig. 6a). In contrast MAO reached the equilibrium within 10 minutes of contact time with a maximum adsorption capacity of 360 mg g^{-1}, as shown in Fig. 6b. This implies that MAO contains more adsorption sites as compared to MAH, as reflected by MAO attaining equilibrium in a very short contact time and having a higher adsorption percentage, even at a MO concentration of 500 mg L^{-1}.

3.2.3 Effect of adsorbent dose. The effect of the adsorbent dose was examined by varying the dose of MAH and MAO from 10 to 50 mg at a 100 mg L^{-1} concentration of the MO dye (chosen to avoid saturation), over the course of one hour. A similar trend was observed for both MAH and MAO, whereas the adsorbent dosage increases the adsorption capacity decreases, as shown in Fig. 7b. A higher adsorbent dose increases the chance of adsorbent particle aggregation with a subsequent decrease in the total surface area of the adsorbent particles. This phenomenon decreases the adsorption capacity when higher dose of adsorbent materials are used. A lower adsorbent dose initiates the dispersion of particles onto the surface of the aqueous solution, exposing all the sites to more dye molecules resulting in a higher adsorption capacity. In terms of percentage adsorption, increasing the adsorbent dose of MAH reaches saturation at a certain point whereas the MAO percentage of

© 2025 The Author(s). Published by the Royal Society of Chemistry

Open Access Article. Published on 15 December 2025. Downloaded on 4/9/2026 11:37:07 PM.
This article is licensed under a Creative Commons Attribution-NonCommercial 3.0 Unported Licence.

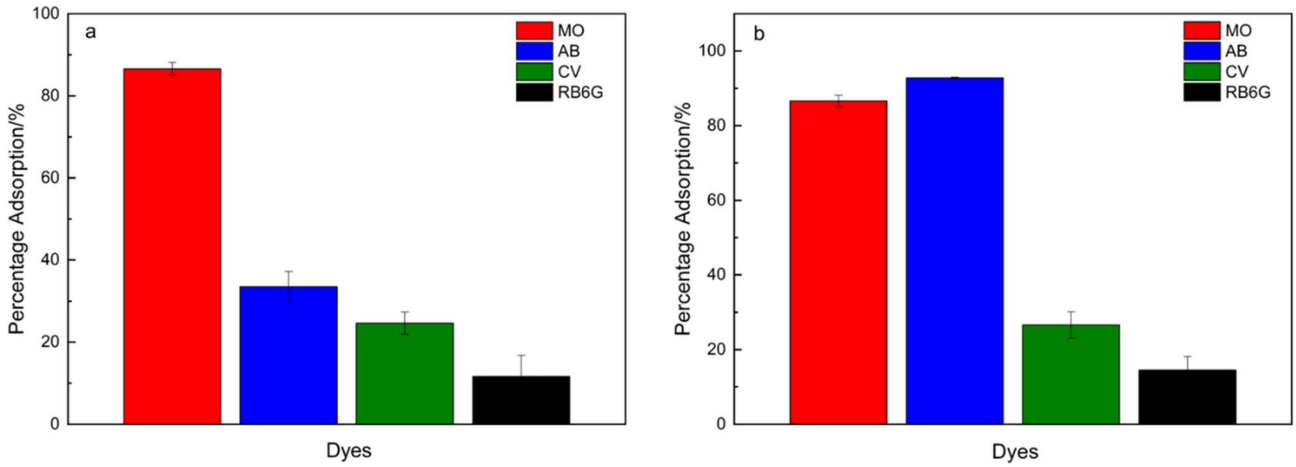

Fig. 5 Percentage adsorption of various cationic and anionic dyes after 60 min using (a) MAH and (b) MAO. Experimental conditions: dye concentration = 200 mg L^{-1}, adsorbent dose = 30 mg, and temperature = 30 °C.

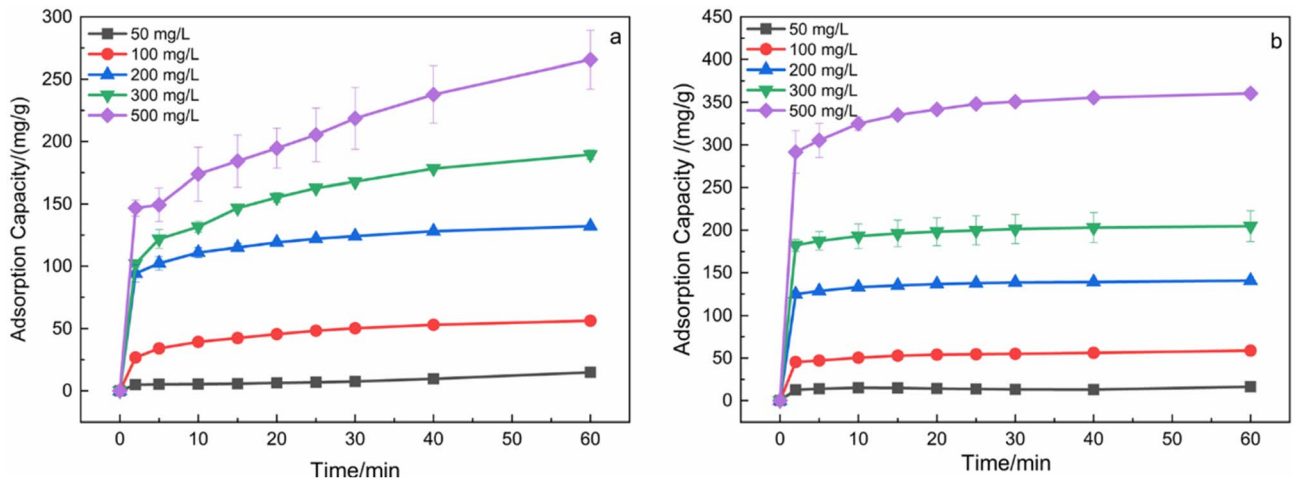

Fig. 6 Effect of contact time and initial concentration of MO on the adsorption capacity of (a) MAH and (b) MAO. Experimental conditions: adsorbent 30 mg and temperature 30 °C.

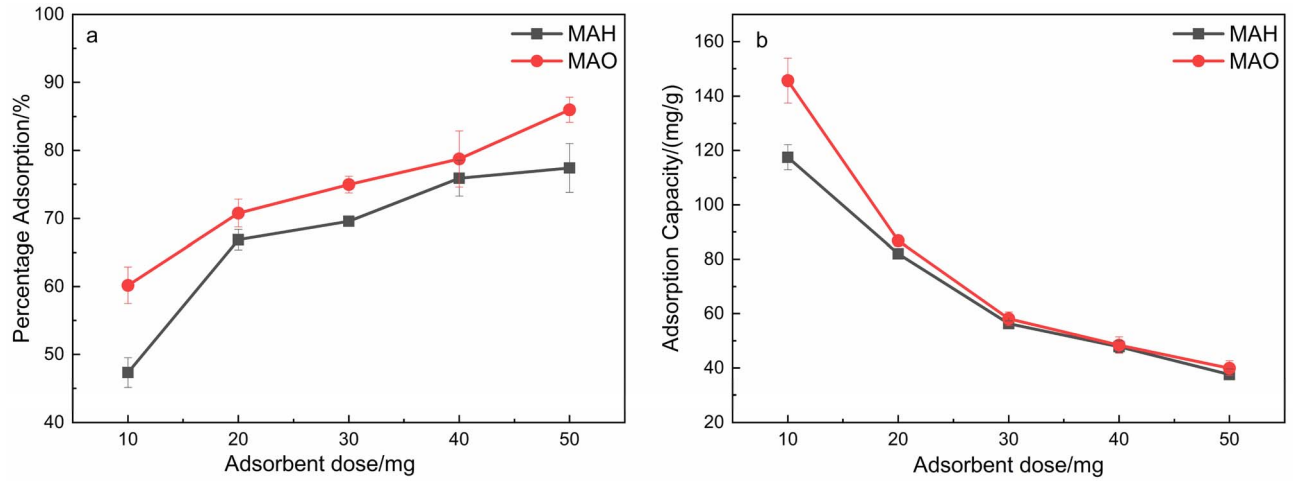

Fig. 7 (a) Percentage adsorption and (b) adsorption capacity of MAH and MAO as a function of adsorbent dose. Experimental conditions: MO dye 100 mg L^{-1}, contact time 1 hour and temperature 30 °C.

© 2025 The Author(s). Published by the Royal Society of Chemistry

Open Access Article. Published on 15 December 2025. Downloaded on 4/9/2026 11:37:07 PM. This article is licensed under a Creative Commons Attribution-NonCommercial 3.0 Unported Licence.

Table 1 Kinetic parameters of MAH and MAO obtained using pseudo-second order kinetic model

Adsorbent	C_o (mg L^{-1})	q_e (calc.)	k_2	R^2
MAH	100	57.60	0.00496	0.991
	200	133.16	0.00487	0.998
	300	192.31	0.00163	0.991
	500	266.67	0.00085	0.977
MAO	100	58.68	0.01377	0.998
	200	141.04	0.01606	0.999
	300	205.34	0.01049	0.999
	500	362.32	0.00331	0.999

adsorption keeps increasing as the adsorbent dose is increased, as shown in Fig. 7a.

3.2.4 Adsorption kinetic model. Different kinetic models were used to study the adsorption rate and mechanism of different MO concentrations (100, 200, 300 and 500 mg L^{-1}) over MAH and MAO. The linearized form of a pseudo-second order rate equation is given in the SI (SEQ-1). The adsorption kinetic studies following the above equation fit well with the experimental data with an R^2 value close to 1. The calculated kinetic parameters for MAH and MAO are listed in Table 1. The experimental values are in close agreement with the values calculated using the pseudo-second order model and the corresponding linear fits are presented in Fig. 8.

3.2.5 Effect of temperature. Temperature plays a key role in physiochemical studies. The adsorption capacity of the material varies with the change in the temperature, which determines whether the adsorption is endothermic or exothermic. Thermodynamic studies were carried out at four different temperatures (288 K, 293 K, 303 K, 308 K) for MAH and MAO. The spontaneity and feasibility of the adsorption were studied using the equations given in the SI (SEQ -2 and 3).

The linear plot of ln K *versus* $1/T$ (Fig. 9) was used to determine ΔH, ΔG, and ΔS from the slope and intercept. The negative ΔG values at all temperatures (Table 2) confirm the spontaneous and thermodynamically favorable nature of the adsorption process.[28] The negative value of ΔH indicates that the process is exothermic, with a decrease in adsorption capacity as the temperature increases suggesting that the interaction between MO and the adsorbents releases energy.[29] The negative value of ΔS indicates a higher order in the adsorption of MO onto MAH and MAO.[30]

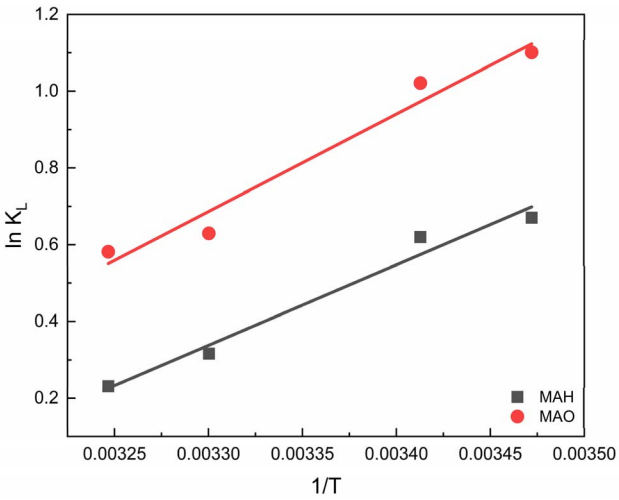

Fig. 9 Linear plot of 1/T *vs.* ln K_L for MAH and MAO.

3.2.6 Effect of pH. The pH of the adsorbate solution plays a vital role in the adsorption process as it affects the surface charge of the adsorbent. At acidic pH, protonation may lead to a positively charged surface, whereas at basic pH, the excess hydroxide ions present on the surface may result in a negative charge. The effect of pH on MO adsorption was evaluated for both adsorbents (Fig. 10). Below pH 4, the structural instability of MO causes variations in its absorption maxima.[31] MAH and MAO exhibit no significant change in adsorption capacity across a pH range of 4 to 10 which suggests that these materials are not sensitive to pH variations and provide stable adsorption sites regardless of changes in surface charge.

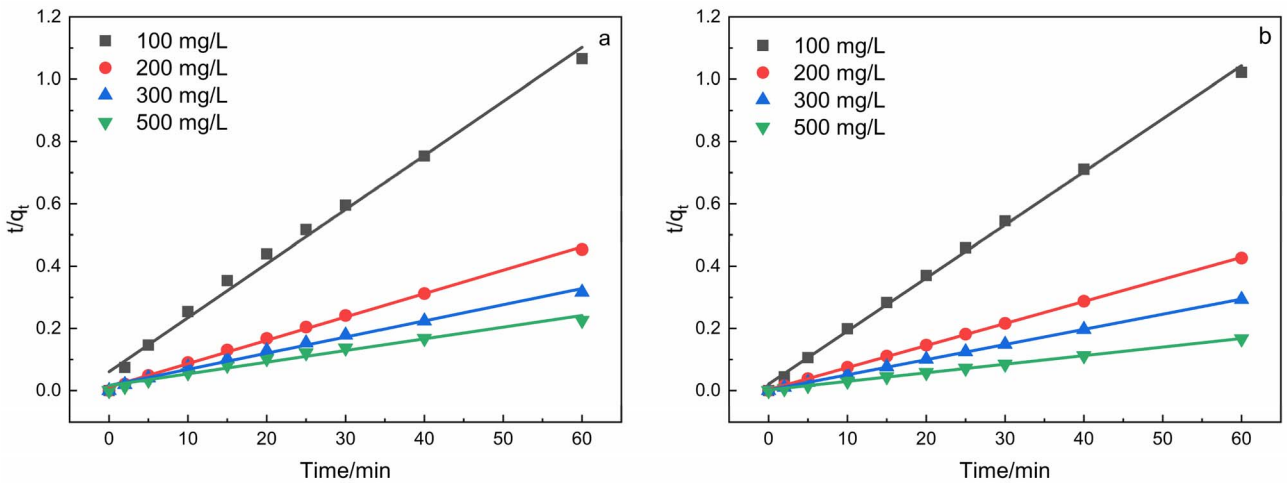

Fig. 8 Linear fitting of the pseudo-second order kinetic model for (a) MAH and (b) MAO.

© 2025 The Author(s). Published by the Royal Society of Chemistry

Open Access Article. Published on 15 December 2025. Downloaded on 4/9/2026 11:37:07 PM. This article is licensed under a Creative Commons Attribution-NonCommercial 3.0 Unported Licence.

Table 2 Thermodynamic parameters of MAH and MAO for the MO adsorption process

Adsorbent	Intercept	Slope	R^2	R (J mol^{-1} K^{-1})	$H°$ (kJ mol^{-1})	$S°$ (J K^{-1} mol^{-1})	$G°$ (kJ mol^{-1})
MAH	−6.57808	2095.70	0.964	8.314	−17.42	−54.69	−1672.95
							−1399.50
							−852.598
							−579.147
MAO	−7.69087	2538.44	0.950	8.314	−21.10	−63.94	−2689.38
							−2369.67
							−1730.26
							−1410.54

3.2.7 Effect of ionic strength. The efficiency of adsorption is significantly influenced by the ionic strength of the solution. The effect of ionic strength was studied using a $NaNO_3$ electrolytic solution that was varied between 0.1 N–0.5 N. Both MAH and MAO showed the same trend where there was a decrease in the adsorption capacity with an increase in ionic strength of the electrolytic solution. This decrease in adsorption capacity is due to the increase in number of anions competing with the MO dye at the adsorption sites, which reduces the amount of MO dye that can be adsorbed on the surface of the adsorbent.[32,33] The effect of ionic strength on MO dye adsorption for both the materials is shown in Fig. 11.

3.2.8 Adsorption isotherms. An adsorption isotherm describes the relationship between the equilibrium adsorption capacity of the MO dye on the adsorbent surface and its equilibrium concentration in solution. This relationship is illustrated by plotting adsorption isotherm graphs, which help characterize the interaction between the MO dye and the adsorbent and allow evaluation of various adsorption parameters. Thus, the adsorption behavior of MAH and MAO was studied using the two commonly used adsorption isotherms, the Freundlich and Langmuir isotherms. The Freundlich adsorption isotherm describes multilayer adsorption, whereas the Langmuir adsorption isotherm describes monolayer formation. The equations for both the linear and non-linear form of the two models are given in the SI (SEQ 4–7).

Adsorption experiments were carried out at varying initial MO concentrations with constant MAH and MAO doses. Equilibrium was achieved at 60 min, and adsorption capacities were calculated. The Langmuir model showed the best fit, with an R^2 value near 1 (Table 3). The maximum adsorption capacities predicted by the Langmuir isotherm plot for MAH (234.19 mg g^{-1}) and MAO (359.71 mg g^{-1}) are in close agreement with the experimentally observed values of 265 mg g^{-1} for MAH and 360 mg g^{-1} for MAO, which indicates monolayer adsorption on a homogeneous surface. The Langmuir and Freundlich isotherm plots are presented in Fig. 12 and S6.

3.2.9 Nitrogen adsorption–desorption isotherms. The surface area of the material plays a key role in adsorption processes. The adsorption–desorption isotherm and the pore size distribution curves of MAH and MAO are presented in Fig. 13. The BET surface area, pore volume and average pore diameter of the materials are presented in Table 4. The BET surface area of MAO is much higher than that of MAH, indicating that MAO has a significantly higher surface area, providing more active sites for the adsorption process. Both

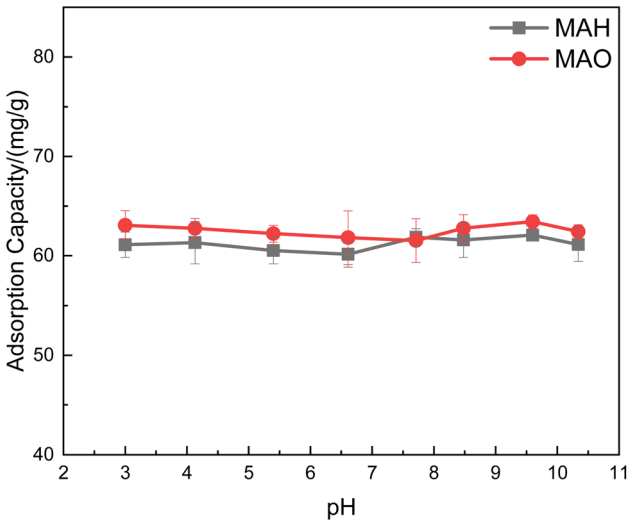

Fig. 10 Effect of pH on MO dye adsorption after 60 min of contact time for MAH and MAO. Adsorbent 30 mg, MO dye 100 mg L^{-1}, contact time 1 hour and temperature 30 °C.

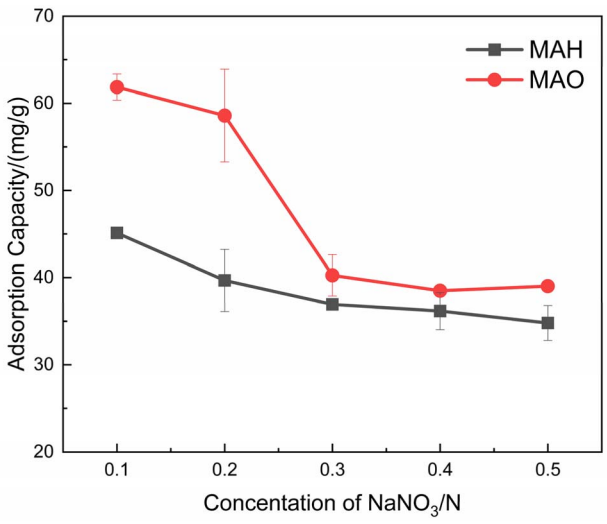

Fig. 11 Effect of ionic strength of MAH and MAO on MO dye adsorption (adsorbent 30 mg, MO dye 100 mg L^{-1}, contact time 1 h, temperature 30 °C).

Open Access Article. Published on 15 December 2025. Downloaded on 4/9/2026 11:37:07 PM. This article is licensed under a Creative Commons Attribution-NonCommercial 3.0 Unported Licence.

Table 3 Adsorption isotherm parameters obtained from linear plots of the Freundlich and Langmuir models

Isotherm model	Constant	MAH	MAO
Langmuir	q_m	234.19	359.71
	K_L	0.02335	1
	R^2	0.99404	0.97732
Freundlich	n	3.7131	0.79435
	K_f	47.037	2.5414
	R^2	0.951	0.924

materials exhibit type IV isotherms, which typically correspond to H_3 hysteresis loops. The average pore size of the materials ranges from 2 to 50 nm which implies a mesoporous structure.[29]

3.2.10 Desorption, regeneration and reusability. Of the two-nanocomposite studied, MAO exhibits a higher adsorption capacity than MAH, making it an excellent adsorbent for the removal of anionic dyes. The reusability of two batches of the MAO material for the adsorption of the MO dye was tested using a 0.1 g sample of MAO and a 200 mg L^{-1} concentration of the MO dye per experiment. After each adsorption cycle, the adsorbed MO was desorbed by washing the material with water and ethanol. The same protocol was repeated over five consecutive adsorption and desorption cycles for both batches. As shown in Fig. 14, the percentage of MO dye adsorption gradually decreased from 100% in the first cycle to 74.36% by the fifth cycle. This decrease in the percentage adsorption happens due to the accumulation of MO dye on the surface and pores of MAO. After the fifth cycle, the first batch of MAO material was restored by washing with 0.1 N HCl, followed by water and ethanol. The material was then dried and reused, resulting in a restored adsorption efficiency of 99.81%, confirming that the acid wash removes the adsorbed MO dye contaminants from the adsorbents surface by cleaning up the occupied adsorption sites. Conversely, the second batch of MAO material was washed with 0.1 N NaOH followed by ethanol and water after the fifth cycle, then dried and reused. This base wash slightly increased the adsorption efficiency to 77.77%. These results demonstrate that the MAO material retains reusability over multiple cycles, and its adsorption capacity can be effectively restored through acid washing, even after several cycles. The absorption spectrum of MO was recorded after desorption using ethanol and compared with that of the pure MO dye before adsorption and is presented in Fig. S7. The absence of any significant change in the absorption behavior before and after adsorption confirms that the nature of the adsorbent-dye interaction is physisorption. This study indicates that both the adsorbent and the adsorbate materials are reusable. We further evaluated the long term stability and reusability of MAO beyond the initial six cycles. After the sixth cycle, the first batch of MAO that had dye adsorbed and had been washed with acid washed was stored for 384 days and then regenerated by washing with 0.1 N HCl, followed by rinsing with water and ethanol, and subsequently drying. The regenerated material exhibited an adsorption efficiency of 99.20%, compared to 99.81% observed immediately after the initial regeneration. These results confirm the excellent long-term stability of MAO and its ability to maintain high adsorption efficiency over extended periods, demonstrating its suitability for multiple regeneration and reuse cycles.

The synthesis of MAH and MAO materials using a high concentration of metal salts produces a uniform crystallinity, resulting in stable and consistent adsorption of the MO dye at different pH levels. These uniform materials demonstrates robust interactions with MO dye under varying environmental conditions. Since the materials exhibit physisorption-type interactions, the adsorption is reversible, allowing for easy desorption of the MO dye. Consequently, both the adsorbate and adsorbent can be reused effectively. Additionally, the MAO material shows excellent reusability; after five adsorption–desorption cycles, acid washing restores its adsorption capacity to nearly 100%. This indicates that dye contaminants are effectively removed from the adsorption sites, enhancing the material's efficiency for repeated use. The important parameters, adsorption capacity, contact time, pH range, number of reuse cycles and temperature, for other available MO dye adsorbents were compared with our studied materials and are presented in Table S2.

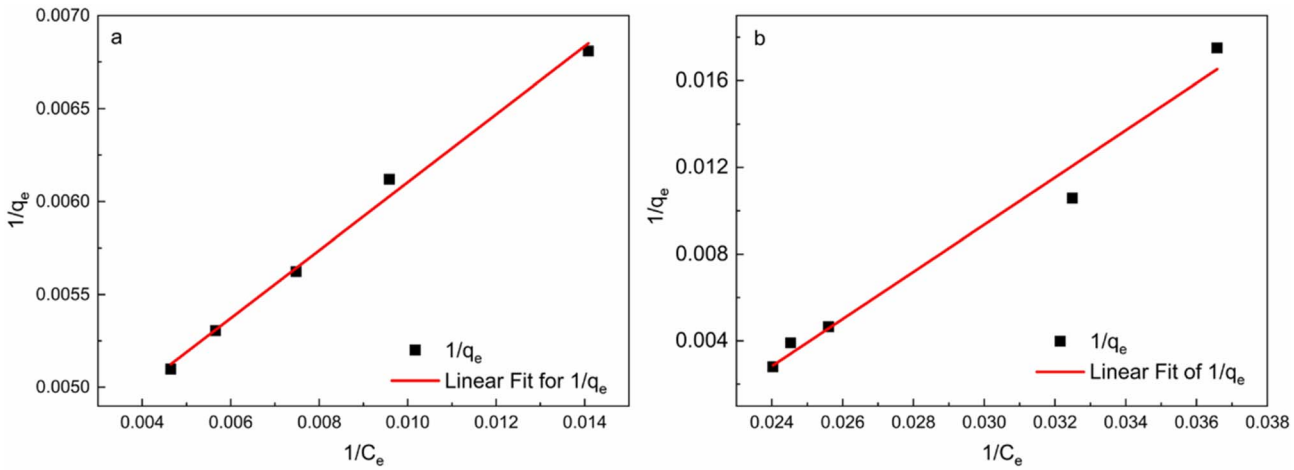

Fig. 12 Langmuir adsorption isotherm linear plots for (a) MAH and (b) MAO.

© 2025 The Author(s). Published by the Royal Society of Chemistry

Open Access Article. Published on 15 December 2025. Downloaded on 4/9/2026 11:37:07 PM.
This article is licensed under a Creative Commons Attribution-NonCommercial 3.0 Unported Licence.

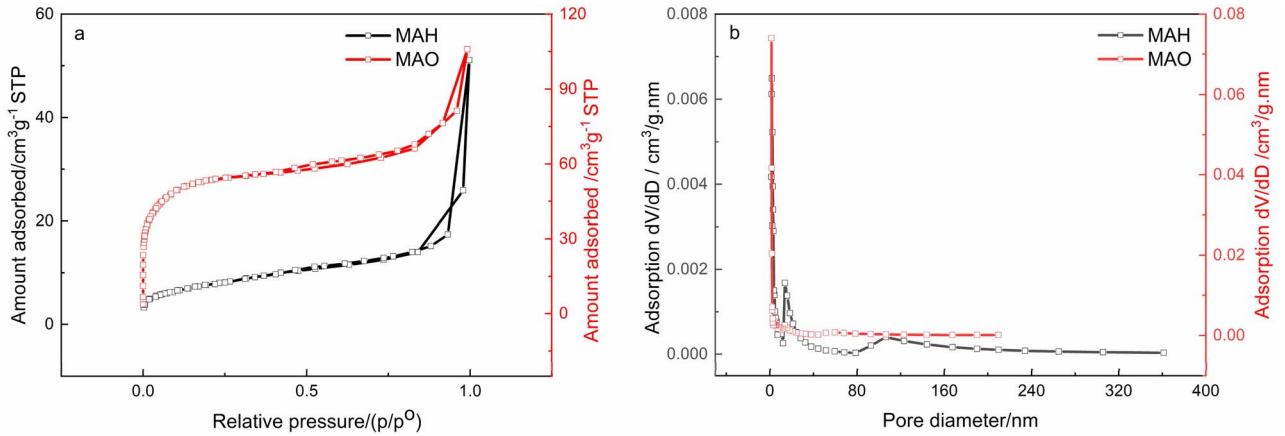

Fig. 13 (a) N_2 adsorption–desorption isotherms and (b) pore size distribution curves of MAH and MAO.

3.2.11 Adsorption mechanism. To elucidate the adsorption mechanism of anionic dyes on MAH and MAO, XRD, SEM with EDX and zeta potential measurements were performed before and after dye adsorption (Fig. S8). Zeta potential measurements indicated that MAH and MAO possess positive surface charges of +9.6 mV and +29.0 mV, respectively, with the more positive value for MAO. After the adsorption of methyl orange (MO), the zeta potentials shifted to −11.9 mV (MAH) and −5.5 mV (MAO), confirming electrostatic interactions between the anionic dye and the positively charged surfaces, along with partial ion exchange with the interlayer anions. SEM analysis after MO adsorption (Fig. S9) showed that the overall morphology of both MAH and MAO remained unchanged, indicating that adsorption occurs primarily on the surface and within the interlayers without altering the particle shape or size. EDX mapping further confirmed successful dye adsorption through the presence of nitrogen (N), sodium (Na), and sulphur (S) signals characteristic of MO in the MO-adsorbed MAH and MAO materials (Fig. S10).

The XRD patterns of the dye-loaded layered double hydroxide (MAH) show the same basal spacing as the material before dye adsorption regardless of the dye type, as shown in Fig. 15a. This finding indicates that the bonding of the dye primarily occurs due to the surface interactions which involve electrostatic interactions between the negatively charged group of the dye with the positively charged layers of the MAH-containing metal ions (Mg^{2+} and Al^{3+}). A schematic representation of the interaction between the MO dye and MAH/MAO is shown in Scheme 2. MAH has hydroxyl groups on the surface with which the azo functional groups (–N=N–) and aromatic rings of the MO dye can form hydrogen bonds which do not interrupt the layered structure. This adsorption mechanism was confirmed from calculations of the basal spacing of the material before and after adsorption where no significant change was observed. Thus, the anionic dye is adsorbed through a combination of electrostatic interactions, hydrogen bonding, and weak van der Waals forces.[34,35]

BET adsorption–desorption isotherms were obtained for both the MAH and MAO materials after the adsorption of the methyl orange (MO) dye and are presented in Fig. S11. As expected, the BET isotherms obtained after adsorption of the MO show that the surface area of MAH and MAO decreases from 27.25 $m^2\ g^{-1}$ and 195.56 $m^2\ g^{-1}$ to 13.84 $m^2\ g^{-1}$ and 38.18 $m^2\ g^{-1}$, respectively (Table S3). This significant reduction in surface area further confirms that adsorption primarily occurs on the surface of the materials. All the above results confirm that adsorption occurs on the surface and within the interlayers without significant morphological changes, thus allowing for structural adaptability to different dyes.

Of the two nanocomposites, MAO shows a higher adsorption efficiency than MAH for the MO dye. MAH and MAO possess high surface areas of 27.25 $m^2\ g^{-1}$ and 195.56 $m^2\ g^{-1}$, respectively, along with interlayer negatively charged anions. The higher surface area and greater availability of the positively

Table 4 Surface properties data for MAH and MAO

Adsorbent	BET surface area ($m^2\ g^{-1}$)	Pore volume ($cm^3\ g^{-1}$)	Average pore diameter (nm)
MAH	27.2	0.073	10.9
MAO	196	0.125	4.25

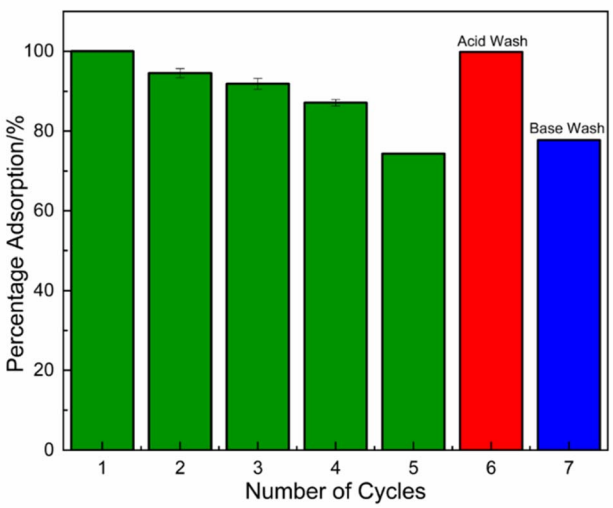

Fig. 14 Reusability of MAO using different washing protocols.

Open Access Article. Published on 15 December 2025. Downloaded on 4/9/2026 11:37:07 PM.
This article is licensed under a Creative Commons Attribution-NonCommercial 3.0 Unported Licence.

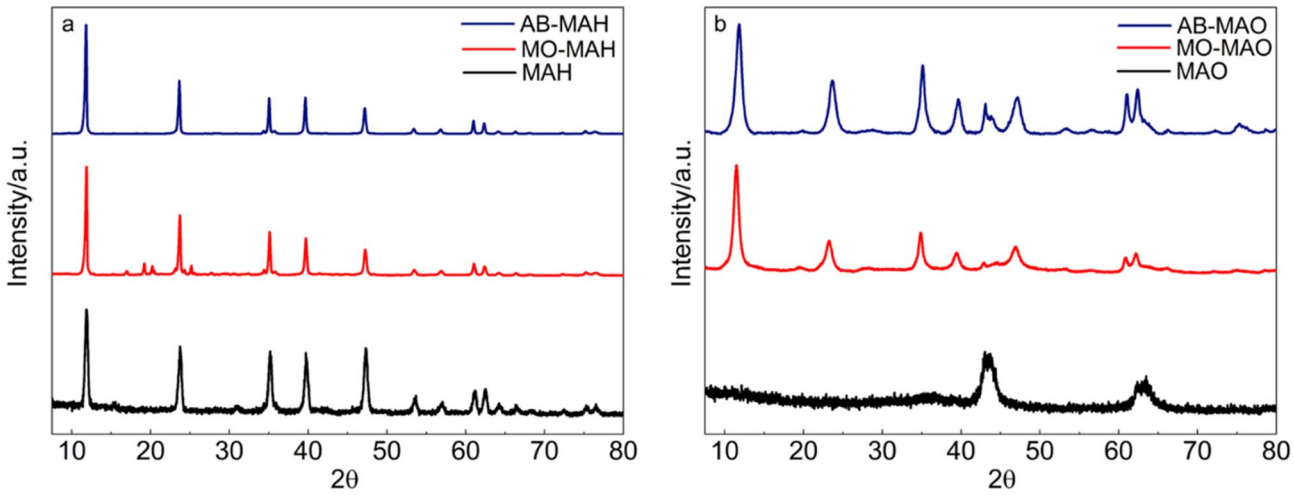

Fig. 15 XRD patterns of (a) MAH and (b) MAO before and after adsorption of the MO and AB dyes.

charged sites in MAO facilitate stronger electrostatic interactions with anionic dyes, resulting in higher adsorption efficiency as compared to MAH. Thermodynamic analysis further supports this observation. The observed enthalpy changes (ΔH) of -17.42 kJ mol^{-1} for MAH and -21.10 kJ mol^{-1} for MAO, obtained from the linear plot of 1/T *versus* ln K_L, indicate that the adsorption is predominantly governed by weak physical interactions (physisorption). The negative Gibbs free energy (ΔG) values confirm that adsorption is spontaneous. Together, the structural characteristics such as high surface area and interlayer anionic sites, combined with favorable thermodynamic parameters, explain the superior adsorption performance of MAO over MAH.

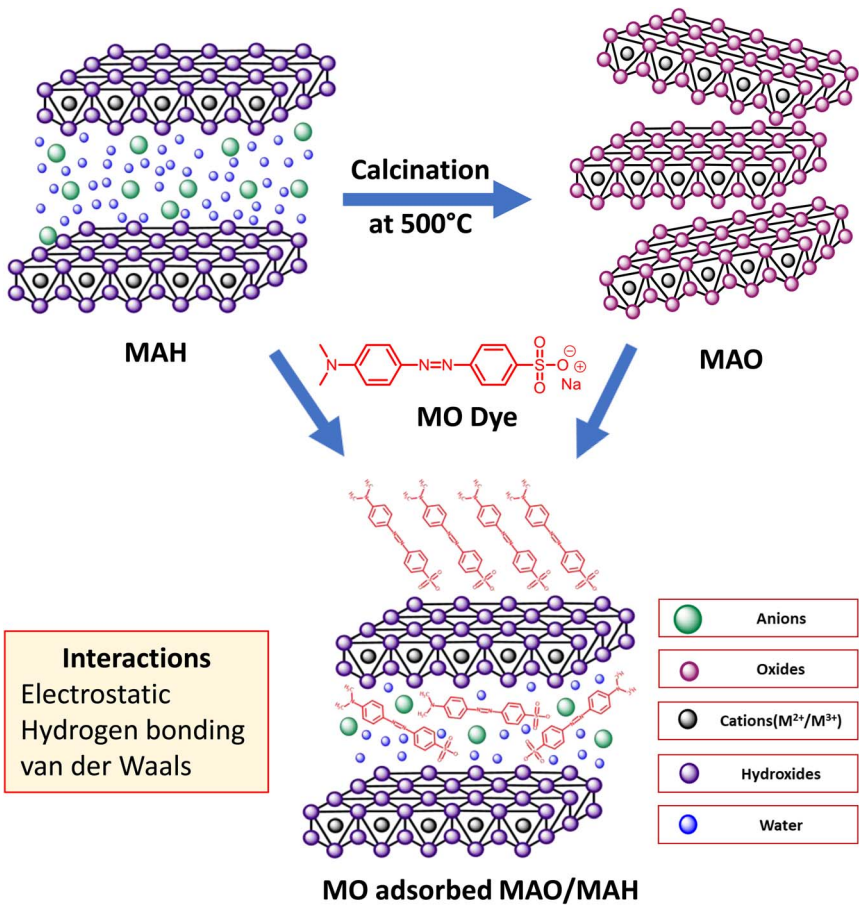

Scheme 2 Schematic representation of the interactions between the LDH/LDO and the MO dye.

© 2025 The Author(s). Published by the Royal Society of Chemistry

Open Access Article. Published on 15 December 2025. Downloaded on 4/9/2026 11:37:07 PM. This article is licensed under a Creative Commons Attribution-NonCommercial 3.0 Unported Licence.

3.2.12 Memory effect. Layered double hydroxides (LDHs) exhibit a unique property known as the "memory effect," which allows their structure to be regenerated and reused even after calcination. The reconstruction of the original LDH structure depends on factors such as the calcination temperature and the material's chemical composition. This behavior was observed in MO dye-loaded LDO (MO-MAO), where the layered structure of the LDH was successfully restored due to the memory effect. The XRD patterns of MO-MAO show the reappearance of the characteristic diffraction peaks of MAH at (003), (006), (012), (015), (018), (110), and (113), as shown in Fig. 15b. When exposed to the aqueous anionic MO dye solution, the MO-adsorbed MAO shows the reappearance of the LDH peaks through rehydration and successful intercalation of the MO dye in the interlayers. This process is called the memory effect.[35–37] The *d* spacing parameters of MAH and MAO are presented in Table S1. The XRD peaks of MAO became broader and less intense with lower crystallinity and after adsorption of the MO dye the regenerated LDH structure showed a decrease in average crystallite size compared to the original structure.

One of the most widely studied LDHs, Mg/Al–CO_3 LDH, typically undergoes dehydroxylation and decarbonation at temperatures ranging from 240 to 480 °C which results in the formation of a mixed oxide structure (MgO) and when the calcination temperature exceeds 800 °C a spinel structure ($MgAl_2O_4$) is formed. Layered double oxides prepared through calcination at temperatures between 450 °C and 550 °C can rehydrate into the layered structure under moist conditions or when exposed to aqueous solution containing anions. The two-dimensional layered structure can absorb anions, and the original layered structure is reformed.[38–41] However, rehydration of LDO into LDH typically produces a new LDH structure rather than fully reconstructing the original.[42] Hence, LDO samples should be stored carefully, as rehydration may occur at room temperature under ambient conditions.

In this work, all adsorption studies for MAO were conducted immediately after calcination to prevent structural changes that could influence the material's adsorption behavior. The regeneration of the material was confirmed by analyzing the XRD patterns of the MAO materials after 30 days of storage under ambient conditions (Fig. S12) whilst the change in adsorption capacity was tested up to 15 days from the calcination date, as shown in Fig. S13.

4. Conclusion

This work demonstrates the effectiveness of MAH and MAO as suitable adsorbents for the removal of MO dye from wastewater. Both materials exhibit higher adsorption capacities, with MAH showing a capacity of 265 mg g^{-1} after 60 min and MAO showing a capacity of 360 mg g^{-1} within 10 minutes of contact time. Of the two materials, MAO shows greater efficiency than MAH due to higher surface area of the material. The kinetics of the adsorbents were studied by varying different parameters such as adsorbent dose, adsorbate concentration, temperature, pH and ionic strength. The adsorption capacity of both materials is influenced by temperature which shows the process is exothermic in nature. The interaction between the MO and both adsorbents releases energy, as demonstrated by the obtained negative enthalpy values, which confirms that the process in spontaneous and thermodynamically feasible. When varying the ionic strength, the adsorption capacity decreases with increasing ionic strength, and both materials show uniform and efficient adsorption towards the MO dye across a wide pH range. The adsorption kinetics of both materials follow the pseudo second order model. Study of the isotherms of the adsorbents reveals that both materials fit well with the Langmuir adsorption model indicating that the adsorption occurs on homogenous surfaces. Thus, MAH and MAO are promising adsorbents for the efficient removal of MO dye from wastewater. MAO can be reused for several cycles, and the memory effect of the material was studied at different time intervals. The simple synthetic procedure, high adsorption capacity over a wide pH range, and their reusability will contribute to the practical applications of these materials in wastewater remediation.

Author contributions

Viruthachalam Thiagarajan: conceptualization, funding acquisition, supervision, investigation, methodology, project administration, data curation, resources, formal analysis, validation, visualization, writing—original draft and writing—review and editing. Saleem Reihana Parveen: investigation, methodology, project administration, validation, visualization, data curation, formal analysis, writing – original draft and writing – review & editing.

Conflicts of interest

There are no conflicts of interest to declare.

Data availability

The data supporting this article have been uploaded as part of the supplementary information (SI). Supplementary information: materials and methods, structural data of dye-adsorbed nanocomposites, supporting figures and tables. See DOI: https://doi.org/10.1039/d5ra06650f.

Acknowledgements

V. T. gratefully acknowledges research funding from the Department of Science and Technology, Nanomission, Government of India (Grant No. DST/NM/NB/2018/10(G)), University Grants Commission, India [Grant No. F. 4-5(24-FRP)/2013(BSR)] and MOE-RUSA 2.0 Physical Sciences, Bharathidasan University for their financial support. S. R. P. thanks the University Grants Commission, India [F. No. 82-7/2022(SA-III)] for financial support through UGC-SJSGC fellowship.

Notes and references

1 B. J. Heyde, M. Braun, L. Soufi, K. Lüneberg, S. Gallego, W. Amelung and J. Siemens, *npj Clean Water*, 2025, **8**, 6.

Open Access Article. Published on 15 December 2025. Downloaded on 4/9/2026 11:37:07 PM. This article is licensed under a Creative Commons Attribution-NonCommercial 3.0 Unported Licence.

2 J. Shamshad and R. U. Rehman, *Environ. Sci.: Adv.*, 2025, **4**, 189–222.
3 A. E. Kuyucu, A. Selçuk, Y. Önal, I. Alacabey and K. Erol, *Sci. Rep.*, 2025, **15**, 28835.
4 M. Sofuoğlu, A. E. Kuyucu, K. Erol and F. Gökmeşe, *Gels*, 2025, **11**, 411.
5 S. R. Parveen, J. Gayathri, R. Vishnupriya, R. Suhasini, N. Madaboosi and V. Thiagarajan, in *Water Remediation Using Magnetic Iron Oxide Nanoparticles for Environmental Sustainability*, Springer International Publishing, Cham, 2023, pp. 407–429.
6 R. Suhasini and V. Thiagarajan, in *Nanomaterials for Water Treatment and Remediation*, CRC Press, 2021, pp. 279–308.
7 S. Sarkar and C. Upadhyay, *Catal. Today*, 2025, **445**, 115101.
8 D. Brahma, M. P. Barman, D. Basak and H. Saikia, *Environ. Sci. Water Res. Technol.*, 2025, **11**, 1234–1256.
9 A. Singha Roy, S. Kesavan Pillai and S. S. Ray, *ACS Omega*, 2022, **7**, 20428–20440.
10 S. Natarajan, V. Anitha, G. P. Gajula and V. Thiagarajan, *ACS Omega*, 2020, **5**, 3181–3193.
11 S. Natarajan, R. Naresh and V. Thiagarajan, *ChemistrySelect*, 2020, **5**, 4165–4174.
12 M. A. Ahmed and A. A. Mohamed, *Inorg. Chem. Commun.*, 2023, **148**, 110325.
13 B. Q. Chen, H. Y. Xia, L. K. Mende, C. H. Lee, S. B. Wang, A. Z. Chen and R. K. Kankala, *Adv. Mater. Interfaces*, 2022, **9**, 2200373.
14 Q. Wang and D. O'Hare, *Chem. Rev.*, 2012, **112**, 4124–4155.
15 Z. Z. Yang, C. Zhang, G. M. Zeng, X. F. Tan, H. Wang, D. L. Huang and K. Nie, *J. Mater. Chem. A*, 2020, **8**, 4141–4173.
16 L. Lv, Z. Yang, K. Chen, C. Wang and Y. Xiong, *Adv. Energy Mater.*, 2019, **9**, 1803358.
17 A. A. Altalhi, E. A. Mohamed and N. A. Negm, *Energy Adv.*, 2024, **3**, 2136–2151.
18 H. Ye, S. Liu, D. Yu, X. Zhou, L. Qin, C. Lai and L. Xiang, *Coord. Chem. Rev.*, 2022, **450**, 214253.
19 T. Hou, L. Yan, J. Li, Y. Yang, L. Shan, X. Meng and Y. Zhao, *Chem. Eng. J.*, 2020, **384**, 123331.
20 G. Mascolo and M. C. Mascolo, *Microporous Mesoporous Mater.*, 2015, **214**, 246–248.
21 S. G. Intasa-Ard and M. Ogawa, *J. Solid State Chem.*, 2023, **317**, 123664.
22 Z. Yan, B. Zhu, J. Yu and Z. Xu, *RSC Adv.*, 2016, **6**, 50128–50137.
23 W. Zhou, Q. Tao, J. Pan, J. Liu, J. Qian, M. He and Q. Chen, *J. Mol. Catal. A: Chem.*, 2016, **425**, 255–265.
24 K. K. Ramasamy, M. Gray, H. Job, D. Santosa, X. S. Li, A. Devaraj and Y. Wang, *Top. Catal.*, 2016, **59**, 46–54.
25 M. Shabanian, M. Hajibeygi and A. Raeisi, in *Layered Double Hydroxide Polymer Nanocomposites*, Woodhead Publishing, 2020, pp. 77–101.
26 Y. Zou, X. Wang, F. Wu, S. Yu, Y. Hu, W. Song and X. Wang, *ACS Sustain. Chem. Eng.*, 2017, **5**, 1173–1185.
27 S. M. Waly, A. M. El-Wakil, W. M. Abou El-Maaty and F. S. Awad, *RSC Adv.*, 2024, **14**, 15281–15292.
28 M. Zubair, N. Jarrah, M. S. Manzar, M. Al-Harthi, M. Daud, N. D. Mu'azu and S. A. Haladu, *J. Mol. Liq.*, 2017, **230**, 344–352.
29 I. Clark, J. Smith, R. L. Gomes and E. Lester, *J. Environ. Chem. Eng.*, 2019, **7**, 103175.
30 R. R. Shan, L. G. Yan, K. Yang, S. J. Yu, Y. F. Hao, H. Q. Yu and B. Du, *Chem. Eng. J.*, 2014, **252**, 38–46.
31 G. Sriram, A. Bendre, T. Altalhi, H. Y. Jung, G. Hegde and M. Kurkuri, *Chemosphere*, 2022, **287**, 131976.
32 W. Yao, S. Yu, J. Wang, Y. Zou, S. Lu, Y. Ai and X. Wang, *Chem. Eng. J.*, 2017, **307**, 476–486.
33 H. Zaghouane-Boudiaf, M. Boutahala and L. Arab, *Chem. Eng. J.*, 2012, **187**, 142–149.
34 K. El Hassani, B. H. Beakou, D. Kalnina, E. Oukani and A. Anouar, *Appl. Clay Sci.*, 2017, **140**, 124–131.
35 J. Mittal, *J. Environ. Manage.*, 2021, **295**, 113017.
36 Y. Li, Z. Xia, T. Zhan, M. Mao, N. Ma and W. Dai, *Langmuir*, 2025, **41**, 12140–12149.
37 L. Lu, Z. Wu, B. Bi, H. Zhang and A. Shahab, *J. Water Process Eng.*, 2024, **63**, 105418.
38 M. Mokhtar, A. Inayat, J. Ofili and W. Schwieger, *Appl. Clay Sci.*, 2010, **50**, 176–181.
39 H. Pfeiffer, E. Lima, V. Lara and J. S. Valente, *Langmuir*, 2010, **26**, 4074–4079.
40 O. Kikhtyanin, Z. Tišler, R. Velvarská and D. Kubička, *Appl. Catal. A-Gen.*, 2017, **536**, 85–96.
41 L. Jin, X. Zhou, F. Wang, X. Ning, Y. Wen, B. Song and L. Peng, *Nat. Commun.*, 2022, **13**, 6093.
42 W. Xu, M. Mertens, T. Kenis, E. Derveaux, P. Adriaensens and V. Meynen, *Mater. Chem. Phys.*, 2023, **295**, 127113.

© 2025 The Author(s). Published by the Royal Society of Chemistry